4D Synchrotron Tomographic Imaging of Network and Fibre Level Micromechanics in Softwood Paper

F. Golkhosh[a], Y. Sharma[b], D.M. Martinez[c], P.D. Lee[d], W. Tsai[e], L. Courtois[f], D.S. Eastwood[g], A.B. Phillion[h,*]

[a]*School of Engineering, The University of British Columbia, Canada*
[b]*Chair of Biomedical Physics, Department of Physics and School of BioEngineering, Technical University of Munich, Germany*
[c]*Chemical and Biological Engineering, The University of British Columbia, Canada*
[d]*School of Mechanical Engineering, University College London, UK*
[e]*Canfor Pulp Innovation, Canfor Pulp, Canada*
[f]*3Dmagination Ltd., UK*
[g]*School of Materials, University of Manchester, UK*
[h]*Materials Science and Engineering, McMaster University, Hamilton, Canada*

Abstract

A 4D imaging study (3D + time) combining synchrotron tomography with *in situ* tensile testing has been carried out to observe the fibre and network level micromechanics of paper made from northern bleached softwood kraft (NBSK). Quantitative image analysis and digital volume correlation is used to characterize local deformation, the evolution of fibre-fibre contacts, and fibre straightening in a "freeze-dried" handsheet as well as standard handsheets low consistency refined at different refining energies. In the freeze-dried handsheet having low fibre conformability, the results show that deformation at the network level occurs because of fibre straightening and possible inter-fibre bond breakage. Further, significant out-of-plane deformation near the failure regions was observed, which led to auxetic behaviour. In the refined handsheets, a strong inverse correlation is seen between refining energy, thickness expansion, and the number of broken fibres. The use of out-of-plane strain norms is proposed as a method to determine network efficiency (i.e. the ratio of the network's elastic modulus to that of the constituent fibres) as well as the relative contribution of fibre pull-out to the overall failure of the handsheet.

Declaration of interest: None

Keywords: 4D imaging, X-ray tomography, paper physics, micromechanics, refining, pulp mixtures

1. Introduction

Paper is a complex network of cellulose pulp fibres, fragments, and fillers derived from wood. The advent of digital media has motivated industry to search for novel applications for such a ubiquitous yet interesting material. Recent research has resulted in the development of novel paper-based technologies ranging from flexible electronics [1] and energy devices [2] to biomedical sensors [3]; however continued advancement requires further investigation of the process-structure-property relationships of paper materials, especially related to mechanical behaviour.

The mechanical properties of paper are multi-scale, meaning that such properties are dependent upon the behaviour of the individual constituent fibres (fibre-level), as well as the arrangement of the constituent fibres in the resulting fibre network (network level). The modification of either of these features enables tailoring of properties for specific applications. In general, two main processing steps, low consistency (LC) refining, and mixing of wood species, are used to modify the mechanical properties. LC refining induces changes to the fibre morphology to improve fibre strength and fibre conformability [4]. The mixing of wood species alters the level of inter-fibre bonding while reducing the fraction of expensive and strong softwood fibres by substitution of less expensive hardwood fibres (e.g. eucalyptus) [5]. The deformation of paper ultimately results in fracture, which occurs via a combination of fibre pull-out and fibre breakage [6]. In the former, breakage of the inter-fibre bonds result in fibres being pulled out of the paper network [7]. In the latter, the fibres inside the fracture zone break due to high tension inside their fibre walls [6].

A number of experimental methods have been devised to study paper micromechanics. Kettunen and Niskanen [8] developed a method that involves measuring, on Silicon (Si) impregnated specimens, the extent of inter-fibre bond breakage near the crack-line and the distance that the fibre ends are extended from the crack-line to characterize fibre structure damage. The use of Si enhanced the contrast of newly created surfaces in order to identify inter-fibre bond or fibre failures. Zhang [4] utilized this method to compare the effect of wet straining and refining on the fracture

*Corresponding author
Email address: andre.phillion@mcmaster.ca (A.B. Phillion)

properties of paper and observed that the ratio of damage width to pull-out width may be reflective of the degree of fibre segment activation. Isaksson [9] and Gradin [10, 11] used acoustic emission monitoring to study the onset and evolution of damage in paper sheets with inter-fibre bond breakage as their dominant damage mechanism. The detected acoustic waves were then used to generate a stress-strain curve, as well as to indicate the breakage of inter-fibre bonds.

The classical approach to understanding the tensile strength of paper is through the Page equation [12, 13], a phenomenological relationship in which the mechanical properties and geometry of the constituent fibres as well as the fibre network structure, specifically the relative bonded area and the shear bond strength, are taken into account. In recent years, fracture sensitivity, i.e. the notion that tensile strength is a measure of a paper's ability to concentrate strain energy, has gained increased attention. It has been reported that linear elastic fracture mechanics modified for paper, and a characteristic length defined as the length of the extended fracture process zone (FPZ) are sufficient to describe the fracture resistance for a wide range of paper grades [14, 15, 16]. Coffin et al. [17] reported the existence of a unique curve when a normalized tensile strength was plotted against FPZ.

In this work, 4D X-ray tomographic imaging of paper handsheets during tensile deformation is performed to observe in 3D the slowly-varying evolution of fibre-level properties and network-level micromechanics. 4D imaging refers to imaging in 3D the microstructure evolution of a material while performing a time-dependant analysis such as mechanical deformation. This technique is made possible by recent advances in fast synchrotron X-ray computed tomographic microscopy. 4D imaging has been used to study the combined microstructure and mechanical evolution of many different materials (e.g. [18, 19, 20, 21, 22]), however its application to paper products has been limited. Latil et al. [21] characterized the 3D evolution in fibre orientation of a saturated fibre bundle undergoing compression. Viguié et al. [22] measured hygroexpansion of a multi-layer paper-board experiencing variations in humidity to show that hygroexpnsion is highly dependant on the fibre content of the fibrous layer. This study focuses on obtaining new fundamental insights into deformation and failure mechanisms using a "freeze-dried" handsheet that was specifically designed to enable quantification of fibre and network level micromechanics. Subsequently, the insights gained from the freeze-dried specimen are applied to systematically investigate the effects of refining energies on micromechanics; addressing the industry interest in advancing our understanding of the contribution of inter-fibre bonding to the strength of paper-based products. The use of 4D imaging enables not only a detailed examination of fibre straightening, buckling, pull-out and fracture at the network level, but also unique insight into the motion of individual fibres within a network during tensile deformation.

2. Methods

2.1. Materials:

Four handsheets were created for this study following the TAPPI T205 procedure [23] and using Northern Bleached Softwood Kraft (NBSK) pulp with an average fibre length of 2.5 mm, fibre width of 28 μm and a coarseness of 0.22 mg/m. The first, with an areal density of $\approx$15 g/m^2, consisted of never-dried (i.e. the fibres were collected in the factory as couch trim from a Fourdrinier papermachine) NBSK pulp that was formed into a handsheet using a British handsheet maker and then subsequently freeze-dried. In this sheet, the lumen were preserved due to the freeze-drying process, facilitating fibre segmentation in image post-processing. The second, third, and fourth also utilized never-dried NBSK pulp which was then refined in a pilot scale LC refiner at one of three refining intensities (0, 60, and 100 kWh/t), air-dried at 23°C and a relative humidity of 50% for 24 h after processing, and then formed into handsheets having an areal density of $\approx$60 g/m^2. Table 1 summarizes the process conditions of the four handsheets. Note that the unit kWh/t is a measure of the power input to the motors of the LC refiner minus the power required to circulate the fibres, based on the amount of pulp processed, and represents an indirect measure of the energy expended in cutting and fibrillating the pulp fibres although only a small amount of power is actually consumed by these processes.

Handsheet	**Refining Intensity**	**Drying Method**
1	n/a	freeze-dried
2	0 kWh/t	air-dried
3	60 kWh/t	air-dried
4	100 kWh/t	air-dried

2.2. Specimen Preparation:

All handsheets were cut into dog-bone shaped specimens, 18 mm long with a gauge region 2.8 mm in length by 3.0 mm in width as shown in Fig. 1(left). The freeze-dried specimen was cut using a laser cutter while the refined specimens were cut using a Silver Bullet® paper cutter. The cutting precision was 0.025 mm with a repeat accuracy of < 0.1 mm. The short gauge region was used to ensure that the fracture would occur within the field of view.

The specimens were then placed within an additively manufactured tensile grip shown in Fig. 1(middle). In order to increase the load to a measureable level of $\approx$20 N, four specimens of the same material were tested at the same time (three for the freeze-dried specimen). Rectangular spacers were placed on either side of each specimen using double-sided adhesive. The spacers were used to separate the specimens such that the individual specimens would be easily distinguishable in the 3D datasets. The adhesive layers also provided reinforcement to ensure

that fracture did not occur in the grip area, and to facilitate load transfer between the specimens and spacers. A screw/nut setup was employed to affix the specimens to the tensile grips via application of a compressive load that further reduced the likelihood of fracture occurring in the grip area. Fig. 1(right) shows a photo of a fully assembled and ready-to-test multi-specimen testing sample.

Fig. 1 also shows the global coordinate system used in this study, with x being in-plane in the direction of loading, y being in-plane and transverse to the direction of loading, and z being out-of-plane (through thickness) and transverse to the direction of loading.

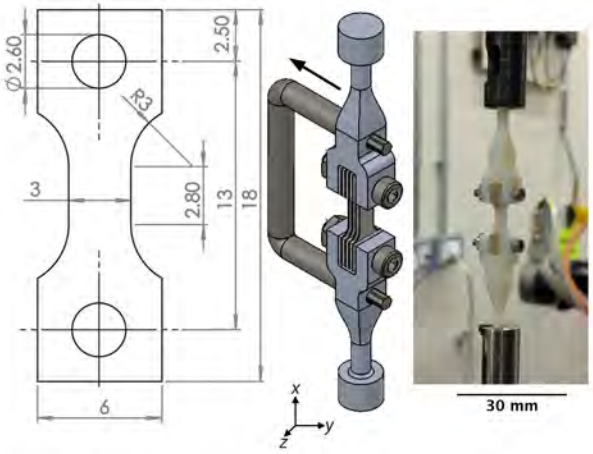

Figure 1: Specimen Preparation: (left) Schematic drawing of the tensile test specimen (units in mm); (middle) CAD drawing of the additively-manufactured grips with multiple specimens inserted and a U-shaped support bracket that was removed prior to mechanical testing; (right) Photo of Experimental setup on the I13 beam-line.

2.3. 4D imaging of Deformation:

The 4D imaging experiments were performed on the I13 beam-line at the Diamond Light Source (Didcot, UK) under pink beam conditions (i.e. all available wavelengths in the 8-30 keV energy range) and absorption contrast mode using a bespoke tensile tester known as the P2R [20] having a load capacity of 500 N and 0.1% repeatibility. Each multi-specimen testing sample was deformed in step-wise increments of 100 μm, with deformation applied at a rate of 100 μm/min followed by a 2-minute hold, followed by acquisition of the 3D image. Specifically, 1800 X-ray projections were acquired in a step-wise fashion using a PCO Edge camera and a 4x objective lens with an exposure of 0.1 s per projection. The total time to acquire each 3D image, having a voxel size of 1.6 μm and a field of view of $4 \times 4 \times 4$ mm^3, was thus 180 s. The 2-minute hold was needed to account for the possibility of stress relaxation that would result in specimen motion and thus blurring in the reconstructed 3D image. In total, twenty to twenty-five 3D datasets were acquired during the deformation process of each testing sample. The actual number of acquired datasets differed for each case, solely dependent upon the material's fracture strain. Once acquired, the datasets were reconstructed [24] using a standard filtered back projection method.

Due to the use of a multi-specimen testing sample, one cannot easily partition the load to individual specimens nor identify the point of load initiation as load transfer may not be equal and torque may be applied to the last-to-fail specimens. These boundary conditions may thus provide a source of error making it impossible to report macro-scale stresses and strains. Similarly, a uniaxial yield stress cannot be determined as it is uncertain if a uniaxial stress state was achieved with a short gauge region; the specimen geometry was determined by the need to constrain deformation and failure to within the field-of-view of the X-ray detector.

2.4. Post-processing and Image Analysis:

Both fibre and network -level image analysis was performed on the acquired datasets. The first step was to crop each dataset to remove all the specimens within the multi-specimen testing sample except the one that fractured second. The first specimen might have had a defect, while the latter two might have experienced a moment arm in addition to tensile load. The second specimen failed in a constrained manner, which best allowed the micromechanics to be captured via X-ray tomographic imaging.

2.4.1. Fibre-level:

To analyze deformation at the fibre-level, each of the cropped freeze-dried 3D datasets was segmented using an enhanced version of the automated fibre segmentation tool developed by Sharma et al. [25]. The original method was based on the assumption that fibres in a paper sheet, and thus the lumen upon which segmentation is based, are all more or less aligned in a single direction. While this is a good assumption for the industrial papermaking process, it is not valid in handsheet specimens due to the fibres being randomly distributed in the in-plane direction. In this study, Sharma's method was extended [26] to account for fibres oriented in each of the three orthogonal directions; this increased the number of voxels identified as lumen by 48%. Fig. 2 provides an example of the 3D visualization of the extracted fibre walls using the lumens labelled by their 3D connectivity; each colour represents a different fibre.

Once the fibres were segmented within the 3D dataset, individual fibre properties could be determined. For this study, two properties were calculated [27]: curl index (also known as tortuosity) and relative contact area. The curl index is defined as the ratio of a fibre's chord length to the distance between the two end points, effectively measuring the degree to which an individual fibre is curled relative to a completely straightened fibre. The relative contact area (RCA) is a property similar to relative bonded area (RBA), but applicable to 3D segmented datasets that can be used to evaluate the evolution of inter-fibre bonding with deformation. While RBA represents the fraction of

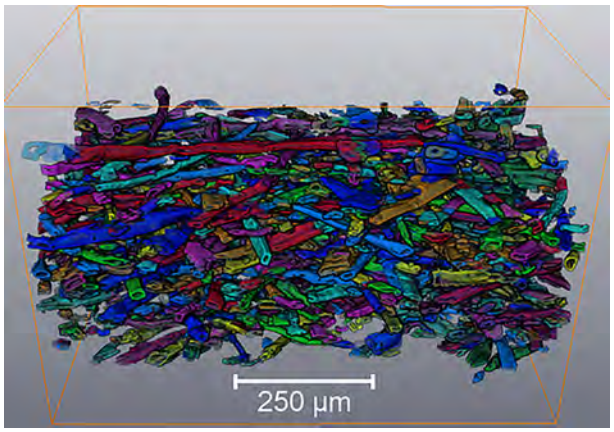

Figure 2: Final 3D visualization of extracted fibre walls in the freeze-dried specimen using lumens labelled by their 3D connectivity. Each colour represents a different segmented fibre.

bonded area between the fibres within a fibre network, RCA represents the fraction of a segmented fibre's surface that is bonded with the remaining fibre network. Thus, RCA represents the fraction of fibre bonding at the fibre-level.

Note that it was not possible to calculate RBA at the network-level as this necessitates the segmentation of all individual fibres within a paper specimen, which is virtually impossible with the currently-available tools. Since the contact area of fibres in digitized volumes also depends on the resolution of the dataset, determination of RBA might anyways not represent the true fibre contact areas; Sorumen et al. [28] showed that nanotomography is required to directly image bonding area. The RCA is useful as a comparative analysis by considering how it changes for an individual fibre at different stages of deformation. Furthermore, while an attempt was made to also quantify the number of contacts and free fibre segment lengths, the complexity of the data-set did not allow for these metrics to be reliably extracted with present image analysis techniques. Finally, as the three refined specimens were not freeze-dried, they did not contain un-collapsed lumens and thus it was not possible to apply this fibre segmentation tool to quantify deformation at the fibre-level.

2.4.2. Network-level:

To quantify the deformation within the handsheet specimens at the network-level, digital volume correlation (DVC) [29] was utilized. DVC, like 2D digital image correlation represents a non-contact method to quantify local strains during deformation; however, DVC can be used to compute an entire 3D displacement field from a volumetric dataset, followed by computation of both localized strain fields and averaged quantities. The DVC method compares the grey-scale value of a deformed 3D dataset against a reference volume, and requires that the two datasets be roughly aligned with each other in order to remove any effects of translation on the calculation of strain fields.

For the present study, the initial, undeformed cropped 3D dataset was used as the reference volume. The correlation process was then carried out by performing a set of linear mapping transformations on a manually chosen sub-volume, containing the fracture region or near to it and that was visible throughout the time series of datasets, in order to quantify displacement vector fields that best transform the deformed dataset back into the initial dataset. As discussed by Bay [30], the inverse displacement vectors are computed to reduce errors when performing DVC calculations on multiple 3D datasets. Finally, the strain tensors were computed using Lagrangian descriptors.

The aforementioned methods used in this investigation are summarized in the flow chart provided in Fig. 3. To begin with, a set of 3D images was obtained by synchrotron X-ray tomographic imaging, and *in situ* tensile testing. Each dataset was subsequently reconstructed using the standard filtered back projection algorithm and then cropped to a single specimen from within the multi-specimen testing sample. Then, the Avizo® image analysis software was used to register the obtained deformed volumes with respect to the reference volume, as well as filter and binarize the data for subsequent analysis. Registration was performed by first applying a manual registration process to achieve a close match between the two datasets followed by applying Avizo's automated registration tool to refine the registration. For the freeze-dried specimen only, the enhanced automated fibre segmentation tool was also applied to the binarized data to segment individual fibres inside both the deformed and reference volumes, and to calculate the curl index and RCA of the segmented fibres. For all four specimens, the registered data was then used by the VicVolume® DVC software for strain field analysis.

2.4.3. Quantifying Through-Thickness Deformation:

As a means to quantify the through-thickness deformation experienced by different specimens during the tensile deformation process, the norm of the out-of-plane strain field, N_z [31], was calculated for each of the acquired 3D datasets analyzed via DVC up to the point of peak loading,

$$N_z = \sqrt{\sum_{ij} {\varepsilon_z^{ij}}^2} \tag{1}$$

where ε_z^{ij} represents the out-of-plane strain at location ij with i and j representing the x and y coordinates in the plane of the specimen. N_z thus represents a characteristic measure of the accumulated through-thickness deformation at each stage of the deformation process.

3. Results and Discussion

First, the experimentally measured loads are presented and discussed to provide a macro-scale overview of the deformation process. Second, the 3D datasets obtained during deformation of the freeze-dried specimen containing a large number of un-collapsed fibres with open lumens

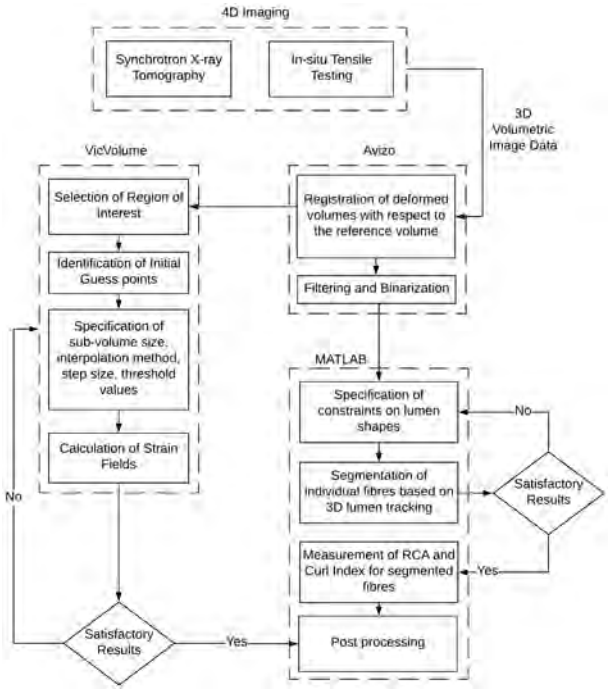

Figure 3: Flow-chart showing data collection and analysis workflow.

are qualitatively and quantitatively analyzed to provide fundamental insight on the network-level and fibre-level micromechanics. Third, the effect of refining on network-level micromechanics is examined. Finally, the network efficiency is discussed in terms of the evolution in N_z for each paper specimen. All of the fracture events occurred within the gauge region of the dog-bone specimen and within the field-of-view of the acquired 3D datasets. Please note that some samples contained areas of yellow/brown discolouration after the 4D imaging, indicating that the intensity of the X-ray beam may have damaged some of the handsheets, potentially diminishing their strength.

3.1. Evolution in Measured Loads

Fig. 4 shows the load evolution during cross-head displacement in the x direction of all four multi-specimen testing samples. As can be seen, the load peaked at 32 N for the testing sample refined at 100 kWh/t at $\Delta x = 1400$ μm, followed by an abrupt drop in load, corresponding to the fracture of one or more of the individual specimens in the multi-specimen setup. The multi-specimen testing samples refined at 0 kWh/t and 60 kWh/t exhibited peak loads of 19 and 21 N at $\Delta x = 1200$ μm, respectively, while the freeze-dried testing sample exhibited a peak load of 8.5 N at $\Delta x = 1000$ μm.

In terms of the deformation process, the significant drop in load after the peak value can be associated with failure of either one or more of the individual specimens in the multi-specimen testing sample. Further, the multi-specimen design resulted in non-typical post-yield behaviour for paper, i.e. the expected strain hardening in the force-displacement plot is missing. It is observed that there is a slight increase in the load at displacements post-peak load for the samples refined at 0, 60, and 100 kWh/t, after which, the load drops to zero. This behaviour is associated with the subsequent deformation and failure of the remaining specimens within the sample, as well as a deformation mechanism known as the parallel chain mode within a single specimen when some chains fail under the displacement-controlled load and some still hold. In contrast, there was no observed post-peak increase for the freeze-dried testing sample, suggesting that the individual specimens likely fractured simultaneously in the tensile grip. Finally, the load drop in the freeze-dried sample was not abrupt like the refined samples, but dropped rather smoothly. This difference is attributed to the fibre pull-out occurring during deformation, a feature of the freeze-dried specimens, but not the refined specimens where the observed fracture method was inter-fibre fracture.

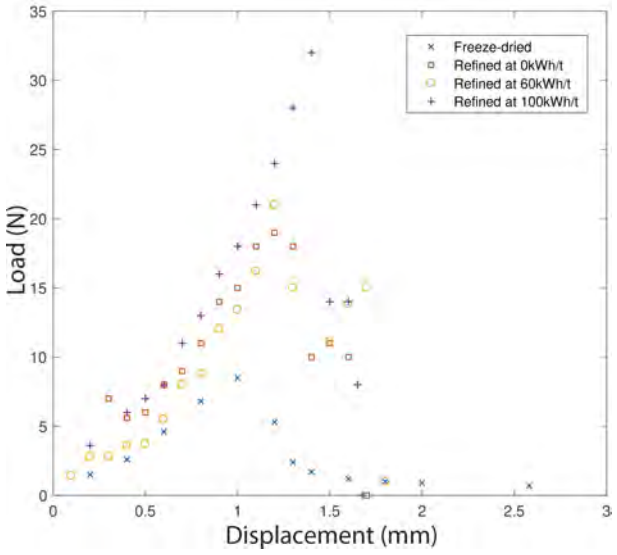

Figure 4: Evolution in measured load as a function of P2R tensile tester cross-head displacement in the x direction for each of the multi-specimen testing samples.

3.2. Micromechanics of the Freeze-Dried Specimen

3.2.1. Network-level Qualitative Observations

Fig. 5 shows the (1) front (x-y) and (2) side (x-z) views of the freeze-dried specimen in the (a) reference state and (b)-(d) after tensile displacementsw (Δx) of 1200, 1600, and 2580 μm. By comparing these images, the fibre network evolution resulting from tensile deformation can be observed. First, between Fig. 5(a)-1 and Fig. 5(b)-1, it seems that the fibres have become more visible, especially in the bottom of the image at $\Delta x = 1200$ μm. This change in contrast can be associated with detachment of surface fibres from the rest of the specimen. Second, the initial signs of fracture are already evident in the lower region of Fig. 5(c)-1, at $\Delta x = 1600$ μm. As can be seen, there is a large area near the bottom left quadrant of the specimen appearing to be less dense, especially when compared to

the reference state in Fig. 5(a)-1. This is made further evident in Fig. 5(d)-1, with $\Delta x = 2580$ μm, as there are a large number of fibres at the bottom of the specimen that seem to have aligned in the loading direction, indicative of fibre pull-out. Although a ductile rupture zone was not observed during the deformation process, failure in this specimen was identified at $\Delta x = 1200$ μm based on the drop in measured load seen in Fig. 4. Fibre pull-out in the freeze-dried specimen was expected and has been observed previously via 2D microscopy since the freeze-drying process results in extremely weak inter-fibre bonds due to a reduction in the Campbell effect [32], as well as low constituent fibre conformability resulting from a lack of additional refining.

A comparison between the side-view images of Fig. 5(a)-(c) shows a significant increase in specimen thickness with increasing deformation. The thickness expansion was most pronounced at the bottom of the specimen, coinciding with the failure region. A further increase in deformation resulted in local reduction of specimen thickness, as can be seen when comparing Fig. 5(c)-2 and Fig. 5(d)-2. The thickness reduction is associated with the constituent fibres being pulled out of the specimen during increased deformation. This can also be seen in Fig. 5(d)-1, where part of the specimen has been removed from the field of view. The observed thickness expansion (i.e. auxetic behaviour) is reported for other sparse fibre networks, such as electrospun materials [33]. In those networks, the behaviour is attributed to the fact that the fibres oriented laterally to the direction of loading experience compressive force, and, therefore, bend outwards. However, the behaviour is contrary to the findings of Verma [34] where it was identified that in paper specimens having weak hygrogen bonding, like freeze-dried specimens, there will not be a significant increase in sheet thickness as the fibres would simply slide past each other, having significant opportunity to occupy the empty spaces. It is likely that the auxetic behaviour is linked to the sparseness of the network. In both electrospun and the freeze-dried sheets, the un-bonded segment lengths are long and prone to bending enabling the auxetic behaviour whereas in dense sheets with weak hydrogen bonding the bending effect is difficult to achieve.

3.2.2. Network-level Quantitative Observations

Fig. 6 shows the in-plane strain fields in the loading direction (ε_x, i.e. the vertical direction of Fig. 5(1)) obtained from DVC analysis of the freeze-dried specimen at displacements of 200, 400, 600, and 1000 μm. As the overall strain fields were relatively homogeneous, these contour plots were taken from the centre plane of the specimen with the red regions representing areas of low in-plane strain, while the yellow regions indicating areas of high in-plane strain greater than 0.08. As can be seen in Fig. 6(a), a narrow band of high in-plane strain is formed at the bottom of the specimen at early stages of deformation. A comparison of the calculated strain fields, Figs. 6(a)-(d), reveals that the magnitude of the in-plane strain in this region increases proportionally to the amount of deformation. This is consistent with the observations made in Fig. 5, where fibre alignment and pull-out were observed at the bottom, left region of the specimen. Consequently, it is seen that the in-plane strain concentrates very early in the deformation process of the freeze-dried specimen to a narrow region of the specimen. This agrees with the findings of Ranger and Hopkins [35] and Borodulina et al. [36] that plastic deformation in paper tends to concentrate along lines that move across the specimen at an angle with respect to the applied external load, similar to shear band formation typically associated with ductile materials although shear bands were not directly observed. Korteoja et al. [37] also obtained similar deformation patterns using back-lit photographs of strained Si impregnated paper specimens, showing that plastic deformation in paper are highly un-uniform. They also observed that the site of eventual fracture can be visually identified long before failure [37], also seen in obtained strain fields shown in Fig. 6.

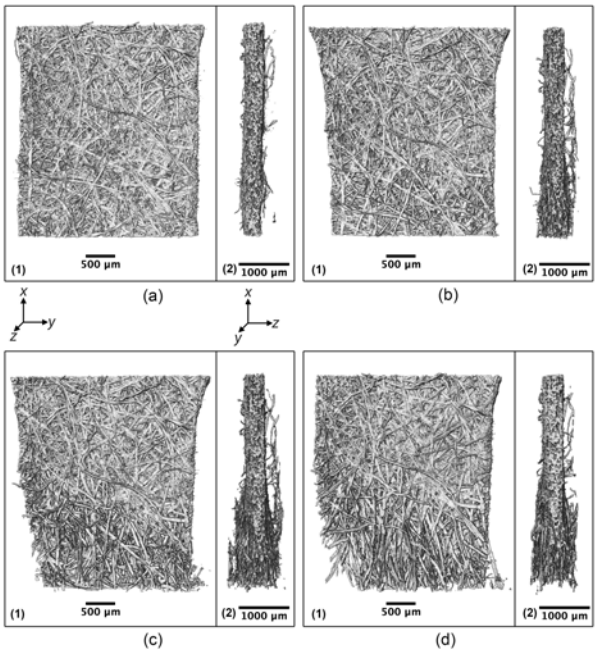

Figure 5: (1) Front (x-y) and (2) side (x-z) visualizations of the freeze-dried specimen in the (a) reference state, and (b-d) after tensile deformations of 1200, 1600, and 2580 μm.

Fig. 7 shows the corresponding out-of-plane strain fields perpendicular to the loading direction (ε_z, i.e. the horizontal direction shown in Fig. 5(2)) also obtained from DVC analysis. Similar to Fig. 6, these contour plots were taken from the centre plane of the specimen with the red regions corresponding to small out-of-plane deformations while the yellow regions corresponding to areas experiencing larger amounts of out-of-plane deformation. In order to facilitate the data visualization seen in Fig. 7, the maximum strain contour has been limited to 0.2; the white regions thus indicate areas with out-of-plane strains greater

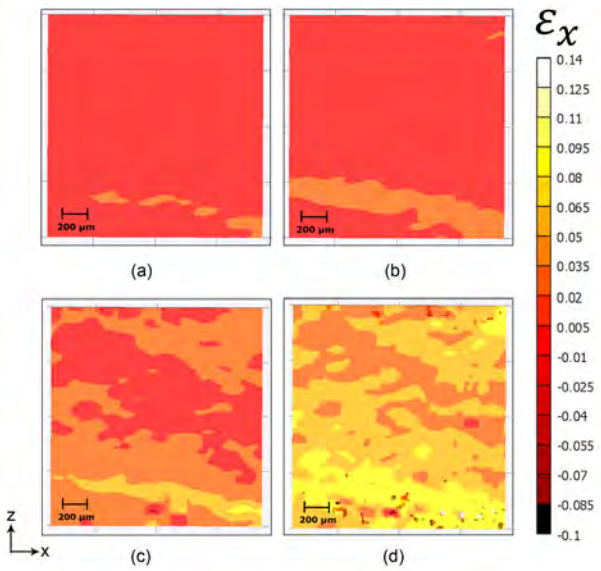

Figure 6: DVC calculated in-plane strain fields in the loading direction (ε_x) at the centre of the freeze-dried specimen for (a-d) Δx = 200, 400, 600, and 1000 μm.

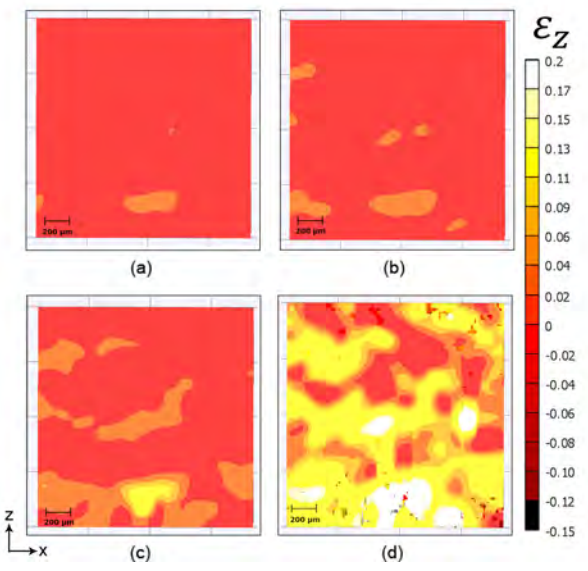

Figure 7: DVC calculated out-of-plane strain fields perpendicular to the loading direction (ε_z) at the centre of the freeze-dried specimen for (a-d) Δx = 200, 400, 600, and 1000 μm.

than 0.2. As can be seen in Fig. 7(a), a region of high out-of-plane strain is formed at the bottom of the specimen, even at early stages of deformation. A comparison of the out-of-plane strain fields in Figs. 7(a)-(d) reveal that the regions of high out-of-plane strain grow in size and magnitude with increasing amounts of tensile deformation. This behaviour is consistent to observations made from Fig. 5, where increasing deformation was associated with the thickness expansion of the specimen, especially in or around the failure region. Thus, it can be concluded that large out-of-plane deformations are concentrated in or around regions of large in-plane deformations. Such out-of-plane thickness expansions have been previously reported in the literature [38, 36].

3.2.3. Fibre-level Qualitative Observations

Fig. 8(a) provides an overview of the fibre structure at Δx = 1200 μm with four manually segmented fibres highlighted in a region of interest. Fig. 8(b) shows three horizontal slices of the same cross-section at: (b)-1 the reference state, (b)-2 Δx = 1000 μm, and (b)-3 Δx = 1200 μm. A comparison between Fig. 8(b)-1 and Fig. 8(b)-2 reveals that after Δx = 1000 μm, only the green fibre has sustained any deformation, while the remaining fibres do not appear deformed nor displaced. By $\Delta x = 1200$ μm, the blue fibre has clearly detached from the red fibre, and also appears to have deformed. The separation between the green and blue fibre has also increased. Although Fig. 8(b) provides some ability to study fibre deformation, it is quite difficult to accurately identify deformation mechanisms using only 2-D cross-sectional slices, as only one cross-section of the fibre is visible at a time. Fig. 8(c) shows a 3D visualization of the four segmented fibres from the selected region of interest: (c)-1 represents the undeformed, reference state, and (c)-2 and (c)-3 represent Δx = 1000 and Δx = 1200 μm. Comparing Fig. 8(c)-1 and Fig. 8(c)-2, it can be seen that the deformation process resulted in the straightening of the green fibre, which led to the subsequent separation with the blue fibre near the middle kink visible in the blue fibre. In Fig. 8(c)-3 it can be seen that after $\Delta x = 1200$ μm, the blue and green fibres lost all connectivity with each other. While there was significant interaction between the blue and green fibres, the blue and yellow fibres remained in contact. When comparing the reference state to the final deformed state, a downward translation is observed with the blue and yellow fibres, suggesting these fibres were in the process of being pulled out. Overall, these observations show that an increase in fibre separation is likely due to the fibre straightening behaviour in low conformed handsheet specimens during the early stages of deformation, consistent with the network-level findings previously mentioned.

Fig. 9 shows a 3D visualization of a set of 18 segmented fibres. The blue fibres were segmented from a deformed specimen at $\Delta x = 200$ μm, while the yellow fibres represent a deformed specimen at Δx = 1000 μm. Due to difficulty of segmenting the exact same fibres within two different volume datasets, the segmentation algorithm selected 18 fibres based on similar identity between the two deformed datasets. As can be seen, the fibres at the bottom left exhibit noticeable movement. Conversely, fibres near the top of the specimen have negligible deformation. This observation is consistent with previous behaviour seen in Figs. 5-7: network-level deformation occurred in the bottom and left region of the specimen; however, it is difficult to accurately characterize fibre-level deformation via qualitative observations. This necessitates further quantitative calculations

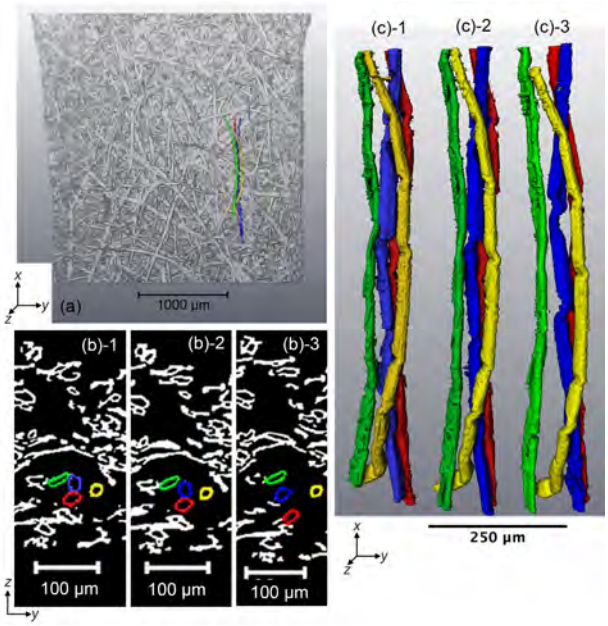

Figure 8: (a) 3D visualization of the freeze-dried specimen at Δx =1200 μm; (b) Cross section of the same specimen and (c) segmented fibres in the region of interest at -1" reference state, -2" Δx =100 μm, and -3" Δx =1200 μm.

such as curl index and RCA measurements.

3.2.4. Fibre-level Quantitative Observations

Fibre Length: Fig. 10(a) shows a plot of the fibre length evolution for the segmented fibres seen previously in Fig. 8 using the same number and colour scheme. The red bars represent the relative change in the fibre lengths between deformation configurations. As can be seen, the relative change in fibre length is minimal. This is expected since the elastic modulus of cellulose is 20 GPa and the applied loads are small. The small values of the relative change in fibre length are mainly associated with fibre movement and deformation that have caused the fibres to move in or out of the field of view.

Relative Contact Area: Fig. 10(b) shows the corresponding evolution in RCA. As seen in the figure below, the RCA is seen to both increase and decrease in the studied fibres. Fibre (1), located at the bottom of the specimen, near the failure region, exhibited the most significant loss in RCA. This observation is consistent with previous observations in Fig. 9, in which the blue fibre lost contact with other fibres, yellow and green, respectively, indicating presence of inter-fibre bond breakage. Fibre detachment can result in a significant increase in fibre-fibre distance, and as such, it is considered to be a contributing factor to the large out-of-plane strains measured inside the observed failure regions. Since some manual segmentation was required for merging volume data between two datasets, it has proved difficult to generalize the change in RCA and possibly inter-fibre bond breakage during the deformation process; however, inter-fibre bond breakage is clearly occurring in the region where fracture occurred.

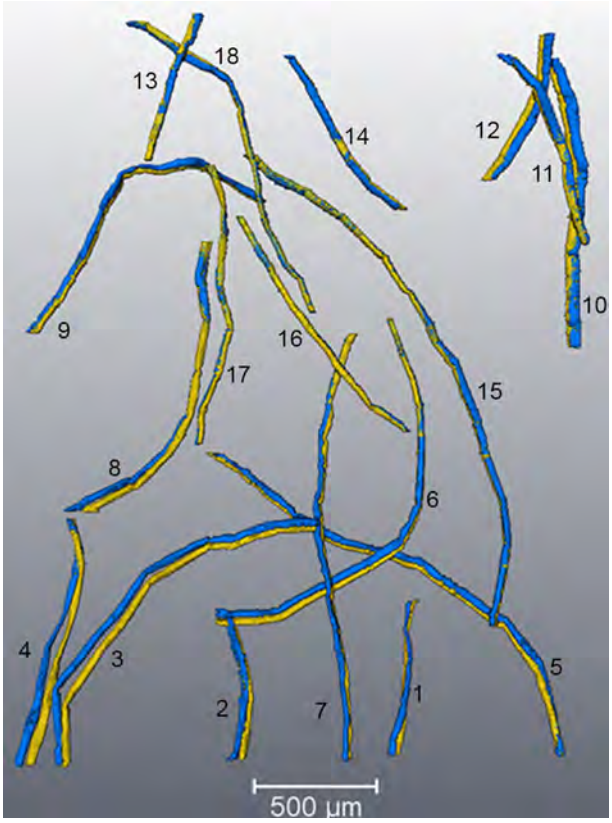

Figure 9: 3D visualization of segmented freeze-dried fibres in the initial configuration (blue) at Δx =200 μm and a deformed configuration (yellow) at Δx =1000 μm. The numbers represent individually-identified fibres.

Curl Index: Fig. 10(c) shows the corresponding evolution in curl index. As can be seen, most fibres exhibit a reduction in curl index, indicative of fibre straightening. This observation is consistent with the expected auxetic behaviour of paper resulting from fibre straightening [39, 38, 34], and the general trends that have been observed for the out-of-plane strain fields. The amount of relative change becomes less negative with corresponding increase in assigned fibre number. As the low numbers are generally assigned to fibres at the bottom of the specimen, the biggest reduction in curl index, and consequently the largest magnitude in straightening, is observed with fibres in or near the failure region. Conversely, in fibres (10) and (13), there is an increase in curl index with increasing deformation, meaning that their contour length has increased. This may be an indication of fibre deflection caused by compressive forces inside the specimen.

Although an estimation of the error in fibre length, RCA, and curl index would seem appropriate, this is not possible as some fibres extend beyond the field of view and the contact is limited to those fibres that we can segment.. Overall, the quantification of the micromechanics observed via 4D imaging of deformation in the freeze-dried specimen provides strong evidence that large amounts of

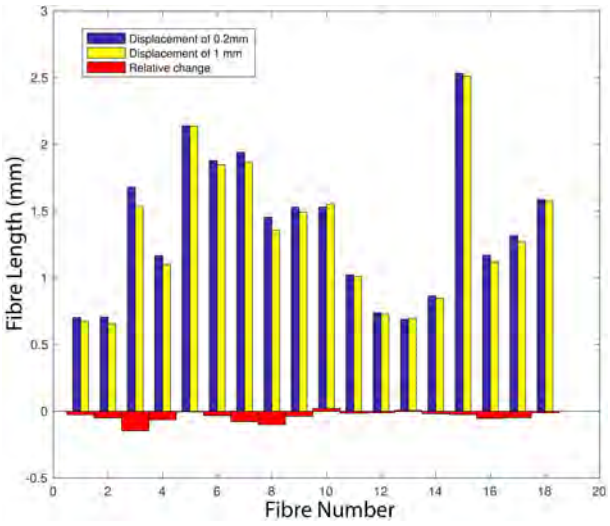

(a)

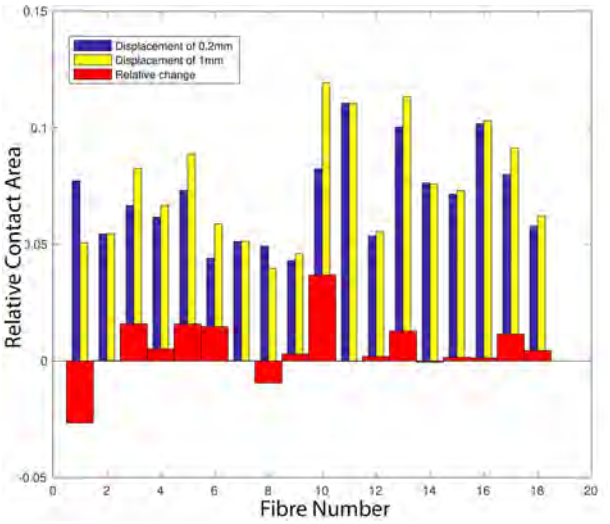

(b)

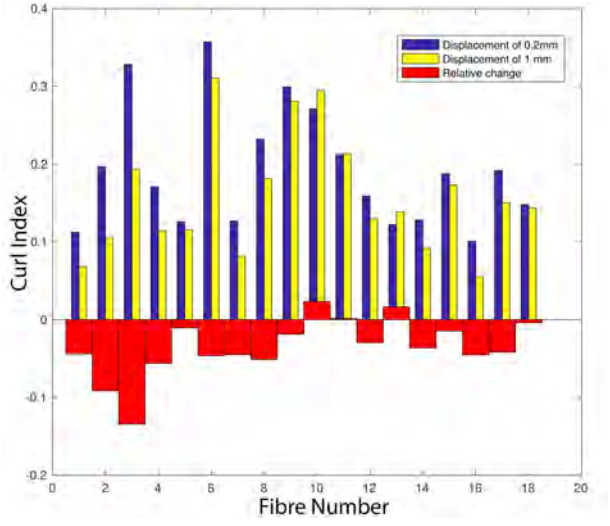

(c)

Figure 10: Quantification of deformation characteristics in the freeze-dried specimen between the initial and configuration (blue) at Δx =200 μm and a deformed configuration (yellow) at Δx =1000 μm; (a) Fibre length comparison; (b) Relative contact area; (c) Curl index. The red bars indicate the relative positive or negative change of each quantity.

fibre straightening, and possible inter-fibre bond breakage, lead to the large out-of-plane strains observed in or around the failure regions. At the fibre-level, relative changes in curl index can be used to quantify fibre straightening inside the paper specimen; while at the network-level, the out-of-plane strain fields are able to identify fibre straightening induced deformation. Thus it is proposed that the application of out-of-plane strain norm provides a simple means to determine the relative contribution of fibre pull-out to the overall failure of a specimen.

3.3. Effects of Refining on Network-level Mechanics

3.3.1. Qualitative Observations

Fig. 11 provides the in-plane (x-y) 3D visualization of each of the four specimens with different refining intensities, namely, freeze-dried, 0, 60, and 100 kWh/t, at the point of fracture to demonstrate how refining energy affects fibre flexibility, free fibre length, and inter-fibre bonding to alter fibre deformation localization, strength and ductility. Beginning with Fig. 11, it can be seen that the freeze-dried specimen exhibits a large amount of fibre-pullout as discussed previously. In contrast, definitive fracture zones are present in the specimens refined at 0, 60, 100 kWh/t, Fig. 11(b)-(d). The amount of fibre breakage seems to be increasing with increasing refining energy, indicating that fibre fracture rather than fibre pull-out occurred and providing evidence that the relative fraction of fibre pull-out occurring during deformation decreases with increasing refining energy. Thus, higher refining energies correspond to stronger paper networks, as known conventionally.

Fig. 12 provides the out-of plane (x-z) 3D visualization of the four specimens. In each, the image on the left shows the specimen in the initial state, prior to deformation, and the image on the right corresponds to the specimen at the point of fracture. The fracture regions that were observed in Fig. 11 are indicated by a dashed-line rectangle for each specimen. As can be seen, there is a decrease in the initial specimen thickness with an increase in refining energy. This can be attributed to conformability, *i.e.* fibre flexibility: with higher refining energies, the fibres become more conformable. In general, flexible fibres show an increase in relative bonding area as compared to more stiff fibres, effectively leading to a more dense paper network [40, 41], and by proxy, a stronger handsheet. Other factors that would also increase densification upon refining include an improvement in bonding due to increased swelling and the presence of fines, which improved the interlocking. The freeze-dried specimen, Fig. 12(a), reveals a significant thickness expansion upon loading from the initial state to failure state. For specimens refined at 0 and 60 kWh/t, Fig. 12(b) and (c), the thickness expansion in the failure region decreases with increasing refining. In addition to increasing fibre conformability, increased refining energy reduces the free fibre lengths i.e. the length of a fibre between two inter-fibre bonds. For the specimen re-

fined at 100 kWh/t, a reduction in thickness is occurring just prior to fracture rather than thickness expansion.

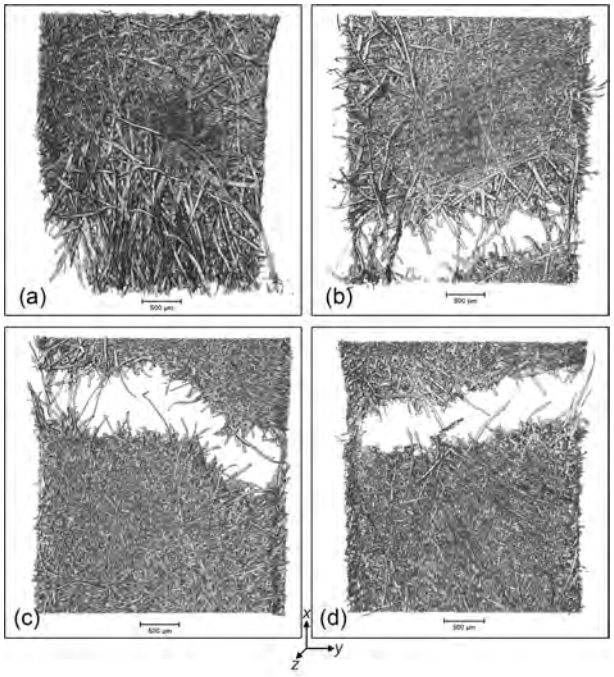

Figure 11: In-plane (x-y) visualizations of fracture surfaces in the (a) freeze-dried specimen and the (b-d) 100% NBSK specimens refined at 0, 60, 100 kWh/t. Note that (a) is the same as Fig. 5(d)

3.3.2. Quantitative Observations

Strain contours from the DVC analysis of the acquired 3D datasets at the centre of all four specimens just at the point of peak load are provided in Fig. 13. The left column of Fig. 13, (a)-1 to (d)-1, shows the DVC calculated in-plane (ε_x) strain fields, while the right column, (a)-2 to (d)-2, show the corresponding out-of-plane (ε_z) strain fields. The large region of high in-plane deformation in the freeze-dried specimen, Fig. 13(a), and discussed previously is also found in the 0 kWh/t -refined specimen, Fig. 13(b). Specifically, there is a band of large in-plane deformation near the top of this specimen and corresponding out-of-plane deformation in regions neighbouring the large in-plane deformations. Conversely, specimens refined at refining energies of 60 and 100 kWh/t, Fig. 13(c) and (d), contain very few regions showing large deformation. This lack of strain localization at high refining intensities is quite clear when comparing the out-of-plane strain fields in Figs. 13(a)-2 to (d)-2 as the extent of high strain regions is decreased with increased refining energy. The results shown in Fig. 13, are consistent with and quantify observations made in Fig. 12, namely, the freeze-dried and 0 kWh/t refined specimens show thickness expansion with tensile deformation, while the specimens refined at 60 and 100 kWh/t show minimal to no thickness expansion with tensile deformation. From these findings, it is hypothesized that the occurrence of regions with high out-of-plane strain concentrations, coinciding with regions of high in-plane strain concentrations, are indicative of inter-fibre bond failure.

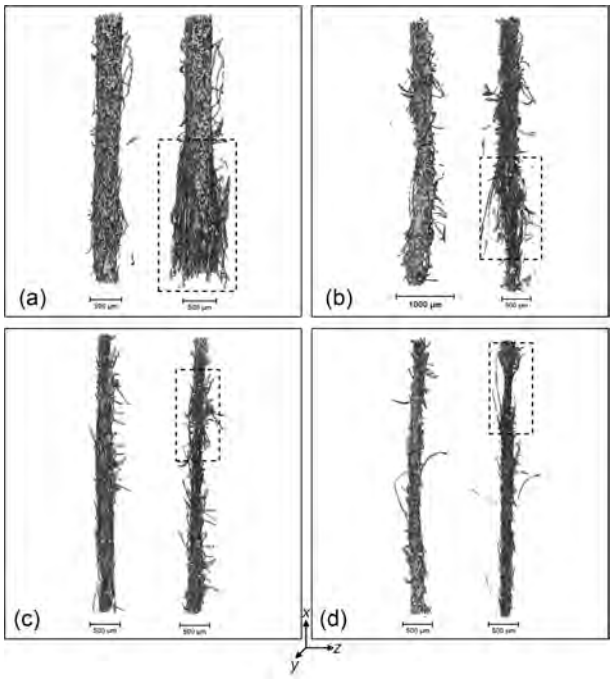

Figure 12: Out-of-plane (x-z) visualizations of the (a) freeze-dried specimen and the (b-d) 100% NBSK specimens refined at 0, 60, 100 kWh/t in the reference and deformed states.

3.4. Network Efficiency

In paper physics, the term network efficiency is a concept that describes the degree to which network-level properties approach fibre-level properties. Fibres having undergone significant refining are known to be efficient [13, 12], because increased refining energy increases inter-fibre bonding and decreases free fibre length. The lack of in-plane deformation seen in Fig. 13(c) and (d) shows that for more efficient paper networks, there is (i) less localization of damage i.e. a more uniform stress distribution before the failure occurs, leading to a more brittle-appearing fracture, and (ii) failure is dominated by fibre breakage rather than pull-out. Borodulina et al. [36] performed particle-level numerical simulations to model deformation in paper networks with varying levels of inter-fibre bonding, and reported that in inefficient networks, or networks with low levels of inter-fibre bonding, high strain regions matched the regions experimentally associated with bond failure; while in efficient networks, or networks with high levels of inter-fibre bonding, did not show this result. They also concluded that it is the occurrence of highly localized in-plane strains due to network inefficiency that led to inter-fibre bond failure, and not vice versa. The present 4D imaging study is in agreement with these prior numerical findings: large out-of-plane strain values are concentrated mainly in and around the failure zone for specimens with inefficient networks, but not for specimens with efficient network structures. Overall, the combination of previous

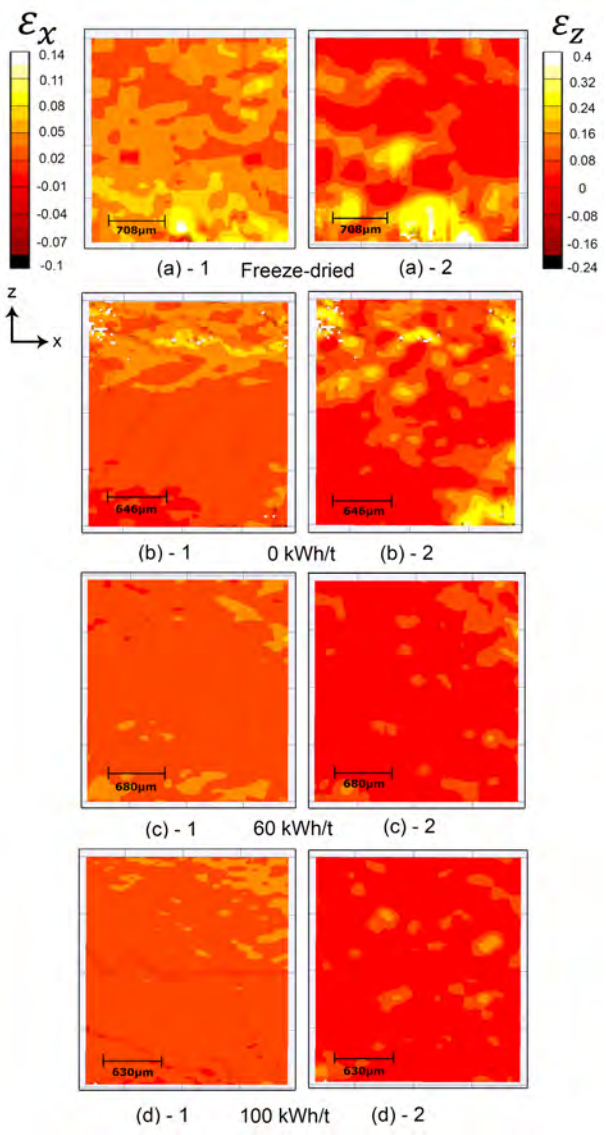

Figure 13: DVC calculated strain fields at the centre of the (a) freeze-dried specimen, and the (b-d) 100% NBSK specimens refined at 0, 60, and 100 kWh/t in the -1 in-plane (x-y) and -2 out-of-plane (x-z) directions at Δx = 1000, 1200, 1200, and 1400 μm respectively.

numerical simulations and current investigations can be used as a criteria to evaluate inter-fibre bond breakage during deformation of paper specimens, and strain localization can be employed as a criterion to evaluate network efficiency.

The plot of strain norm N_z evolution with displacement calculated via DVC analysis for the freeze-dried, and refined specimens is shown in Fig. 14. As can be seen, all curves show the same trend: an increase in N_z occurring with the simultaneous increase of displacement, consistent with auxetic behaviour. Although out-of-plane expansion was not seen in the fracture zone of the 100 kWh/t, Fig. 12(d), expansion was observed outside of the fracture region, thus captured by the strain norm calculation. The increase in the strain norm is small early on, but

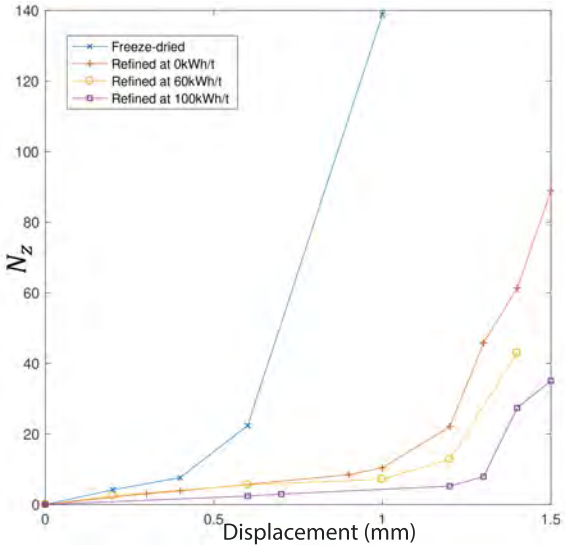

Figure 14: Variation in N_z as a function of cross-head displacement.

increases significantly in the later stages of deformation. This trend is consistent with observations for damage accumulation [9], and Poisson's ratios reported for some paper specimens in the literature [39, 38, 34]. In general, the values for the strain norm increase as the extent of inter-fibre bonding decreases. The differences in N_z between specimens at early stages of deformation is a result of refining energies, and a positive correlation between refining energies and network level efficiency. This translates to lower values of free-fibre length and reduced fibre straightening, and as a result, reduced thickness expansion. Interestingly, the difference in N_z at later stages of deformation where complete fibre detachments were observed were significant. It is a possibility that fibre shortening during refining [42] is causing the observed differences. However, this shortening is minuscule; [41] reported a 3% reduction in fibre length in a 100% softwood specimen refined at 132 kWh/t, which is negligible. It is proposed instead that inter-fibre bond breakage is the main factor responsible for such large differences in the accumulated out-of-plane deformations, as a function of refining. For the specimens refined with lower refining energies, the contribution of complete fibre detachment to N_z becomes significant.

4. Conclusions

In summary, 4D imaging experiments along with digital volume correlation at the network-level and quantitative fibre analysis at the fibre-level have been carried out to characterize deformation mechanisms in a freeze-dried specimen. The developed methodology was then applied to systematically investigate the effects of refining energy on paper networks. From this work, the following conclusions can be drawn:

- In specimens showing considerable fibre pull-out, regions with high in-plane strain concentration also

show high out-of-plane strain concentration.

- As shown in prior studies, fibres inside a paper network both straighten and buckle during deformation. Fibre straightening appears to be more prevalent within fracture regions having high concentrations of out-of-plane strain.
- Fibre straightening followed by possible inter-fibre bond breakage leading to fibre pull-out is responsible for the observed auxetic behaviour of paper networks exhibiting low network efficiency.
- As fibre networks become more efficient with lower free fibre lengths, i.e. those that are subjected to increased refining energy, the contribution from inter-fibre bond breakage and fibre straightening on deformation is reduced.
- In paper networks of high network efficiency, regions of out-of-plane strain do not correspond to regions of high in-plane strain.
- Out-of-plane strain norms can be used as a measure to evaluate network efficiency of paper specimens made from the same pulp.

Overall, 4D X-ray tomographic microscopy is a powerful tool for evaluating the micromechanics of paper deformation. This study on paper deformation has provided the first systematic study of paper micromechanics in 3D. The use of this technology has revealed new insight into deformation mechanisms based on the concept of network efficiency. However, improved methods for segmenting individual fibres are needed to better understand the micromechanics at work at the fibre-level when investigating the effects of refining energy.

5. Acknowledgements

Facilities and research support were provided by Diamond Light Source (Beamtime MT13240-1 on I13-2). The use of the papermaking facilities at The University of British Columbia's Pulp and Paper Centre, as well as the laser cutter at University College London are acknowledged. The authors thank NSERC and Canfor Pulp for financial support, under the NSERC Collaborative Research and Development funding program, as well as the help of C. Parks in proofreading the manuscript. ABP acknowledges use of the facilities and support provided by the Research Complex at Harwell, funded in part by the EPSRC (EP/I02249X/1 & EP/M009688/1).

6. References

[1] D. Tobjörk, R. Österbacka, Paper electronics, Advanced Materials 23 (17) (2011) 1935–1961. doi:10.1002/adma.201004692.

[2] G. Zheng, Y. Cui, E. Karabulut, L. Wågberg, H. Zhu, L. Hu, Nanostructured paper for flexible energy and electronic devices, MRS Bulletin 38 (2013) 320–325. doi:10.1557/mrs.2013.59.

[3] Z. Li, I. D. Tevis, S. Oyola-Reynoso, L. B. Newcomb, J. Halbertsma-Black, J. F. Bloch, M. Thuo, Melt-and-mold fabrication (MnM-Fab) of reconfigurable low-cost devices for use in resource-limited settings, Talanta 145 (May) (2015) 20–28. doi:10.1016/j.talanta.2015.05.002.

[4] G. Zhang, E. Hiltunen, J. Laine, H. Paulapuro, H. Kettunen, K. Niskanen, Comparison of the effects of wet straining and refining on the fracture properties of paper, Nordic Pulp & Paper Research Journal 17 (1) (2002) 45–49.

[5] P. W. Tsai, Developing Mixture Rules for Non-conservative Properties for Pulp Suspension, Master's thesis, The University of British Columbia (2016).

[6] M. Alava, K. Niskanen, The physics of paper, Reports on Progress in Physics 69 (3) (2006) 669–723. doi:10.1088/0034-4885/69/3/R03.

[7] P. Shallhorn, A. Karnis, Tear and tensile strength of mechanical pulps, Pulp and Paper Magazine of Canada 80 (1979) 12.

[8] H. Kettunen, K. Niskanen, Microscopic damage in paper. part i: Method of analysis, Journal of pulp and paper science 26 (1) (2000) 35–40.

[9] P. Isaksson, P. A. Gradin, A. Kulachenko, The onset and progression of damage in isotropic paper sheets, International Journal of Solids and Structures 43 (3-4) (2006) 713–726. doi:10.1016/j.ijsolstr.2005.04.035.

[10] P. Gradin, S. Nyström, P. Flink, S. Forsberg, F. Stollmaier, Acoustic emission monitoring of light-weight coated paper, Journal of pulp and paper science 23 (3) (1997) J113–J118.

[11] P. A. Gradin, D. Graham, P. Nygård, H. Vallen, The use of acoustic emission monitoring to rank paper materials with respect to their fracture toughnes, Experimental Mechanics 48 (1) (2008) 133–137. doi:10.1007/s11340-007-9055-7.

[12] D. Page, A theory for tensile strength of paper, Tappi 52 (4) (1969) 674.

[13] R. S. Seth, D. H. Page, J. Brander, The Stress Strain Curve of Paper, in: The Role of Fundamental Research in Paper Making, Vol. 1, 1981, pp. 421–452.

[14] D. W. Coffin, K. Li, J. Li, Utilization of Modified Linear Elastic Fracture Mechanics to Characterize The Fracture Resistance of Paper, in: 15th Fundamental Resaerch Symposium, Cambridge, 2013, pp. 637–672.

[15] O. Anderson, O. Falk, Spontaneous crack formation in paper, Svensk Papperstidning 69 (4) (1966) 91–99.

[16] B. Donner, An heuristic model of paper rupture, in: Proceedings of fundamentals of papermaking materials-11th fundamental research symposium, 1997, pp. 1215–1247.

[17] D. W. Coffin, A fracture-based description for the development of tensile and tear strength in paper, Journal of Science and Technology for Forest Products and Processes 6 (2018) 29–38.

[18] J. Y. Buffiere, E. Maire, J. Adrien, J. P. Masse, E. Boller, In situ experiments with X ray tomography: An attractive tool for experimental mechanics, Proceedings of the Society for Experimental Mechanics, Inc. 67 (2010) 289–305. doi:10.1007/s11340-010-9333-7.

[19] F. Beckmann, R. Grupp, A. Haibel, M. Huppmann, M. Nöthe, A. Pyzalla, W. Reimers, A. Schreyer, R. Zettler, In-situ synchrotron X-ray microtomography studies of microstructure and damage evolution in engineering materials, Advanced Engineering Materials 9 (11) (2007) 939–950. doi:10.1002/adem.200700254.

[20] C. Puncreobutr, P. D. Lee, R. W. Hamilton, A. B. Phillion, Quantitative 3d characterization of solidification structure and defect evolution in HEL alloys, JOM 64 (1) (2012) 89–95. doi:10.1007/s11837-011-0217-9.

[21] P. Latil, L. Orgéas, C. Geindreau, P. Dumont, S. R. du Roscoat, Towards the 3d in situ characterisation of deformation micromechanisms within a compressed bundle of fibres, Composites Science and Technology 71 (4) (2011) 480–488. doi:10.1016/j.compscitech.2010.12.023.

[22] J. Viguié, P. J. J. Dumont, É. Mauret, S. R. Du Roscoat, P. Vacher, I. Desloges, J. F. Bloch, Analysis of the hygroexpansion of a lignocellulosic fibrous material by digital correlation of

images obtained by X-ray synchrotron microtomography: Application to a folding box board, Journal of Materials Science 46 (14) (2011) 4756–4769. doi:10.1007/s10853-011-5386-y.

[23] Tappi t205 sp-02: Forming handsheets for physical tests of pulp (https://www.tappi.org/content/sarg/t205.pdf) [online] (2005).

[24] R. C. Atwood, A. J. Bodey, S. W. Price, M. Basham, M. Drakopoulos, A high-throughput system for high-quality tomographic reconstruction of large datasets at diamond light source, Philosophical Transactions of the Royal Society A: Mathematical, Physical and Engineering Sciences 373 (2043) (2015) 20140398.

[25] Y. Sharma, A. B. Phillion, D. M. Martinez, Automated segmentation of wood fibres in micro-CT images of paper, Journal of Microscopy 260 (3) (2015) 400–410. doi:10.1111/jmi.12308.

[26] F. Golkhosh, 4D Imaging of Paper: A Novel Method to Characterize Deformation Mechanisms, Master's thesis, The University of British Columbia, DOI: 10.14288/1.0375751 (2018).

[27] N. J. McIntosh, Y. Sharma, D. M. Martinez, J. A. Olson, A. B. Phillion, Estimating the transverse dimensions of cellulose fibres in wood and paper using 2d and 3d microscopy techniques, Cellulose 26 (3) (2019) 2099–2108. doi:10.1007/s10570-018-02231-w.
URL https://doi.org/10.1007/s10570-018-02231-w

[28] T. Sormunen, A. Ketola, A. Miettinen, J. Parkkonen, E. Retulainen, X-ray nanotomography of individual pulp fibre bonds reveals the effect of wall thickness on contact area, Scientific Reports 9 (1) (2019) 4258. doi:10.1038/s41598-018-37380-2.
URL https://doi.org/10.1038/s41598-018-37380-2

[29] B. K. Bay, T. S. Smith, D. P. Fyhrie, M. Saad, Digital volume correlation: Three-dimensional strain mapping using X-ray tomography, Experimental Mechanics 39 (3) (1999) 217–226. doi:10.1007/BF02323555.

[30] B. K. Bay, Methods and applications of digital volume correlation (2008). doi:10.1243/03093247JSA436.

[31] C. D. Meyer, Matrix Analysis and Applied Linear Algebra, 2nd Edition, Society for Industrial and Applied Mathematics, 2000.

[32] W. B. Campbell, The mechanism of bonding, Tappi 42 (12) (1959) 999–1001.

[33] S. Domaschke, A. Morel, G. Fortunato, A. E. Ehret, Random auxetics from buckling fibre networks, Nature Communications 10 (1) (2019) 4863. doi:10.1038/s41467-019-12757-7.
URL https://doi.org/10.1038/s41467-019-12757-7

[34] P. Verma, M. L. Shofner, A. C. Griffin, Deconstructing the auxetic behavior of paper, Physica Status Solidi (B) Basic Research 251 (2) (2014) 289–296. doi:10.1002/pssb.201384243.

[35] A. Ranger, L. Hopkins, The formation and structure of paper, Brit. Paper and Board Makers' Assoc., London UK (1962) 277.

[36] S. Borodulina, A. Kulachenko, G. Sylvain, M. Nygards, Stress-strain curve of paper revisited, Nordic Pulp and Paper Research Journal 27 (02) (2012) 318–328. doi:10.3183/NPPRJ-2012-27-02-p318-328.

[37] M. J. Korteoja, A. Lukkarinen, K. Kaski, D. E. Gunderson, J. L. Dahlke, K. J. Niskanen, Local strain fields in paper, Tappi Journal 79 (4) (1996) 217–223.

[38] P.-P. Post, C. Berger, K. Villforth, H.-J. Schaffrath, S. Schabel, Optical measurement of deformation of paper under tensile load, Nordic Pulp and Paper Research Journal 27 (2) (2012) 313–317.

[39] O. Öhrn, Thickness variations of paper on stretching, Svensk Papperstidning 68 (5) (1965) 141–149.

[40] S. Andersson, Low Consistency Refining of Mechanical Pulp: Process Conditions and Energy Efficiency, Ph.D. thesis, Mid Sweden University (2011).

[41] D. Nugroho, Low Consistency Refining of Mixtures of Softwood & Hardwood Bleached Kraft Pulp : Effects of Refining Power, Master's, Asian Institute of Technologye (2012).

[42] R. P. Kibblewhite, Effects of refined softwood/eucalypt pulp mixtures on paper Properties, Trans. 10th Fundamental Research Symposium (1993) 127–155.